# Supporting Information

## Persistent Photoconductivity Enables In-Sensor Binarization and Reservoir Computing in a Single Organic Phototransistor

Haonan Wang[a,†], Huichen Fan[a,†], Wandi Chen[a], Wenjuan Su[a], Shuchen Weng[a,b], Zhenyou Zou[a,b], Xiongtu Zhou[a,b*], Chaoxing Wu[a,b*], Tailiang Guo[a,b], Yongai Zhang[a,b*]

[a]College of Physics and Information Engineering, Fuzhou University, 350002 Fuzhou, China. E-mail: yongaizhang@fzu.edu.cn.

[b]Fujian Science & Technology Innovation Laboratory for Optoelectronic Information of China, 350100 Fuzhou, China.

[†]Haonan Wang and Huichen Fan contributed equally to this work.

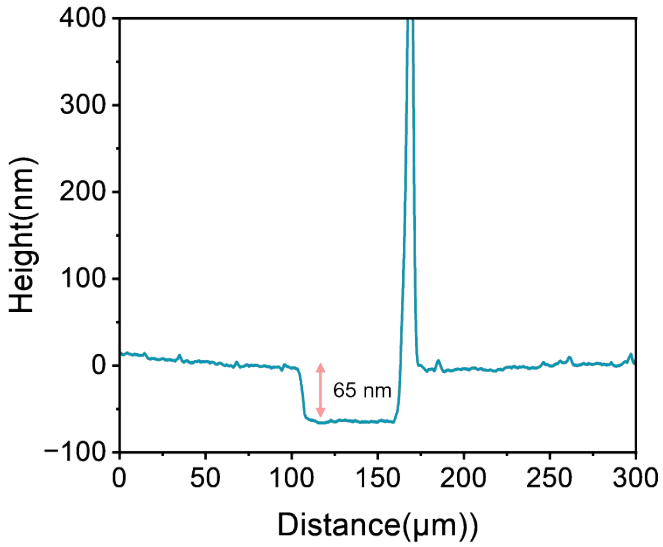


**Fig. S1** Step-height profile of PDVT-10 film (65 nm, prepared at 500 rpm/5 s + 2000 rpm/35 s).

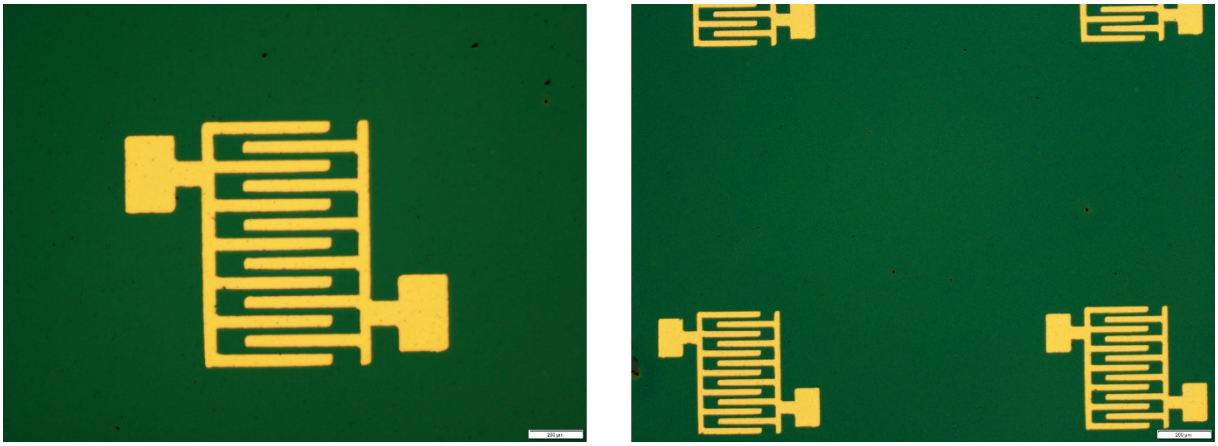

**Fig. S2.** Photographs of fabricated devices.

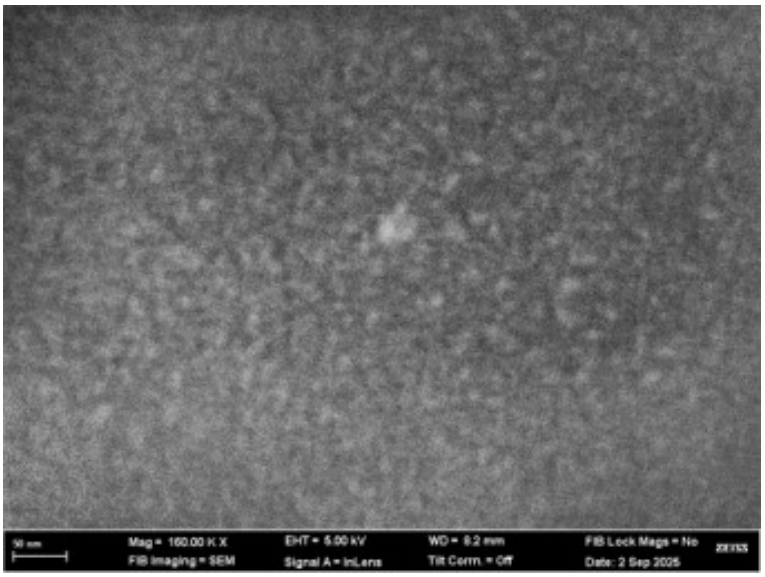

**Fig. S3** Scanning electron microscopy (SEM) images of PDVT-10 films.

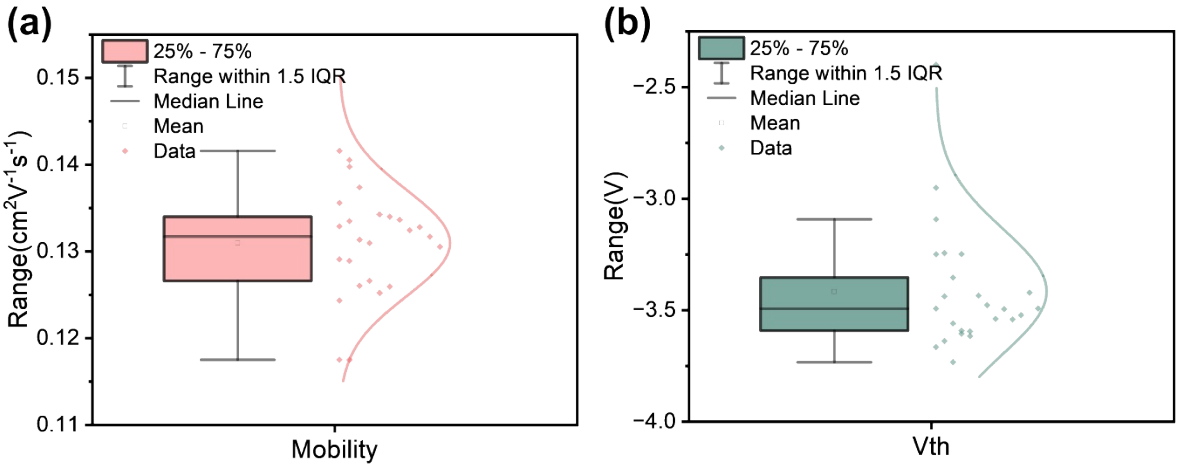


**Fig. S4** Statistical distributions of device parameters. Histograms showing (a) field-effect mobility (μ) and (b) threshold voltage ($V_{th}$) distributions extracted from the transfer characteristics of 25 OPTs from the same sample.

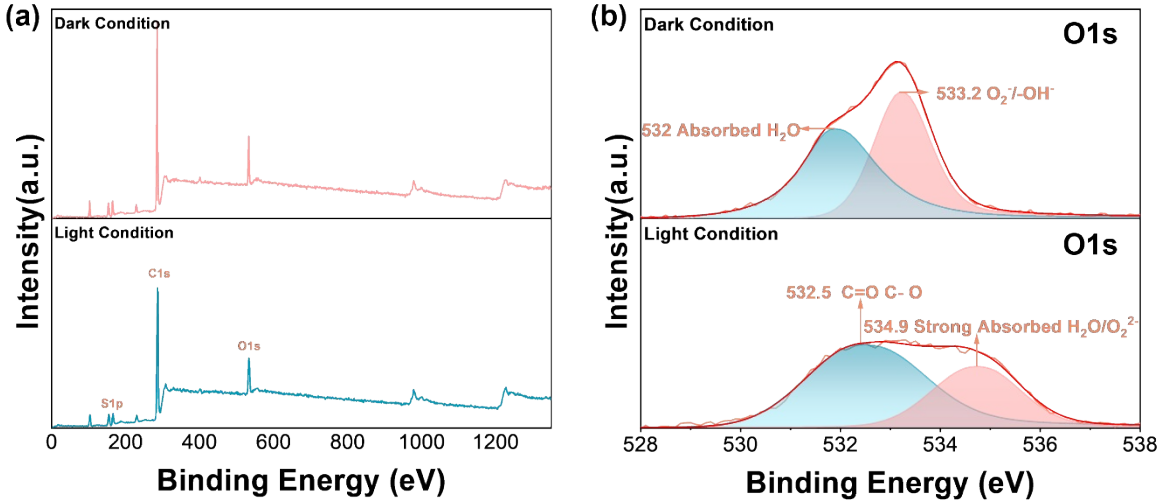


**Fig. S5** X-ray photoelectron spectroscopy (XPS) with in situ illumination. (a) Survey XPS spectrum of PDVT-10 films measured under dark and illuminated conditions, (b) High-resolution C 1s spectra.

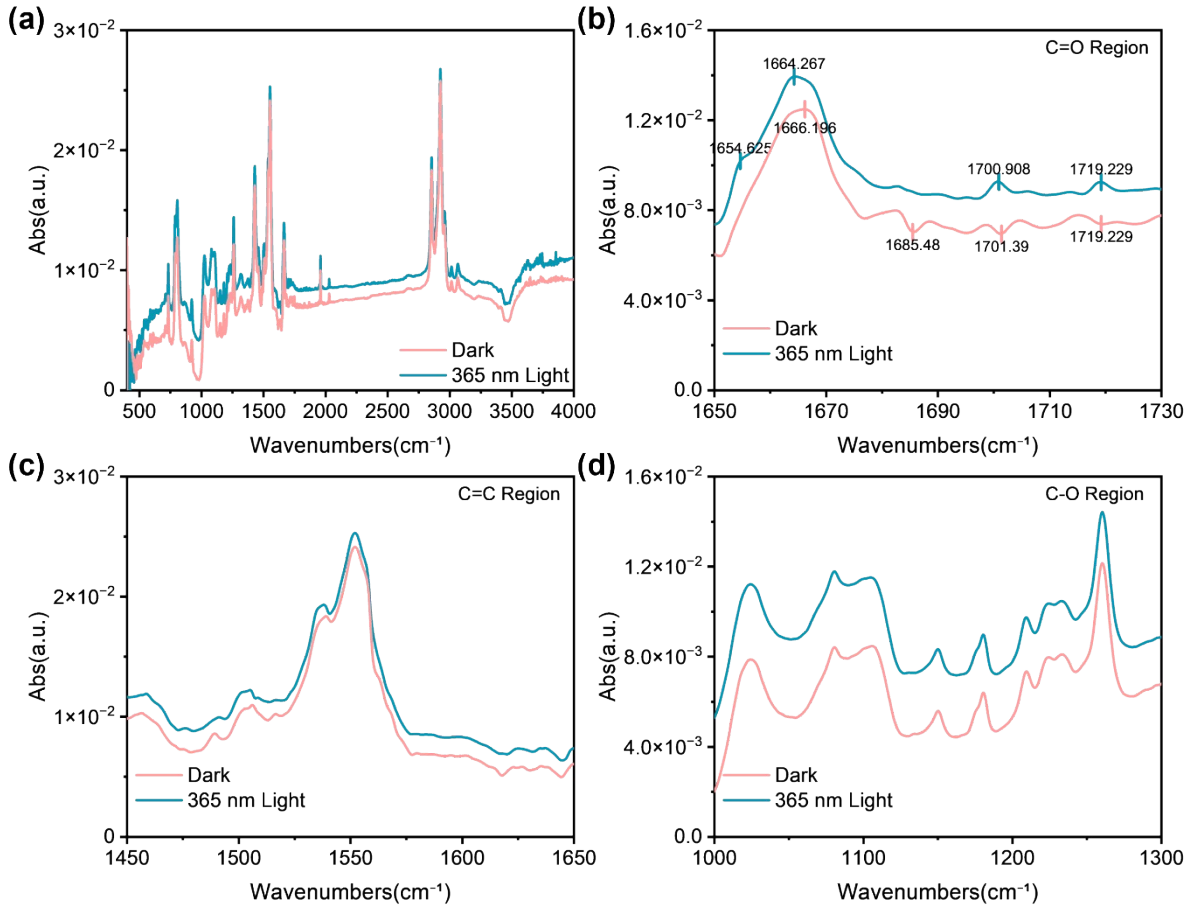


**Fig. S6** Fourier-transform infrared (FT-IR) spectroscopy characterization. (a) Full-range FT-IR spectrum of PDVT-10 films (4000–400 $cm^{-1}$). Enlarged views of characteristic spectral regions: (b) C=O stretching region (1650–1730 $cm^{-1}$), (c) C=C stretching region (1450–1650 $cm^{-1}$), and (d) C–O stretching region (1000–1300 $cm^{-1}$).

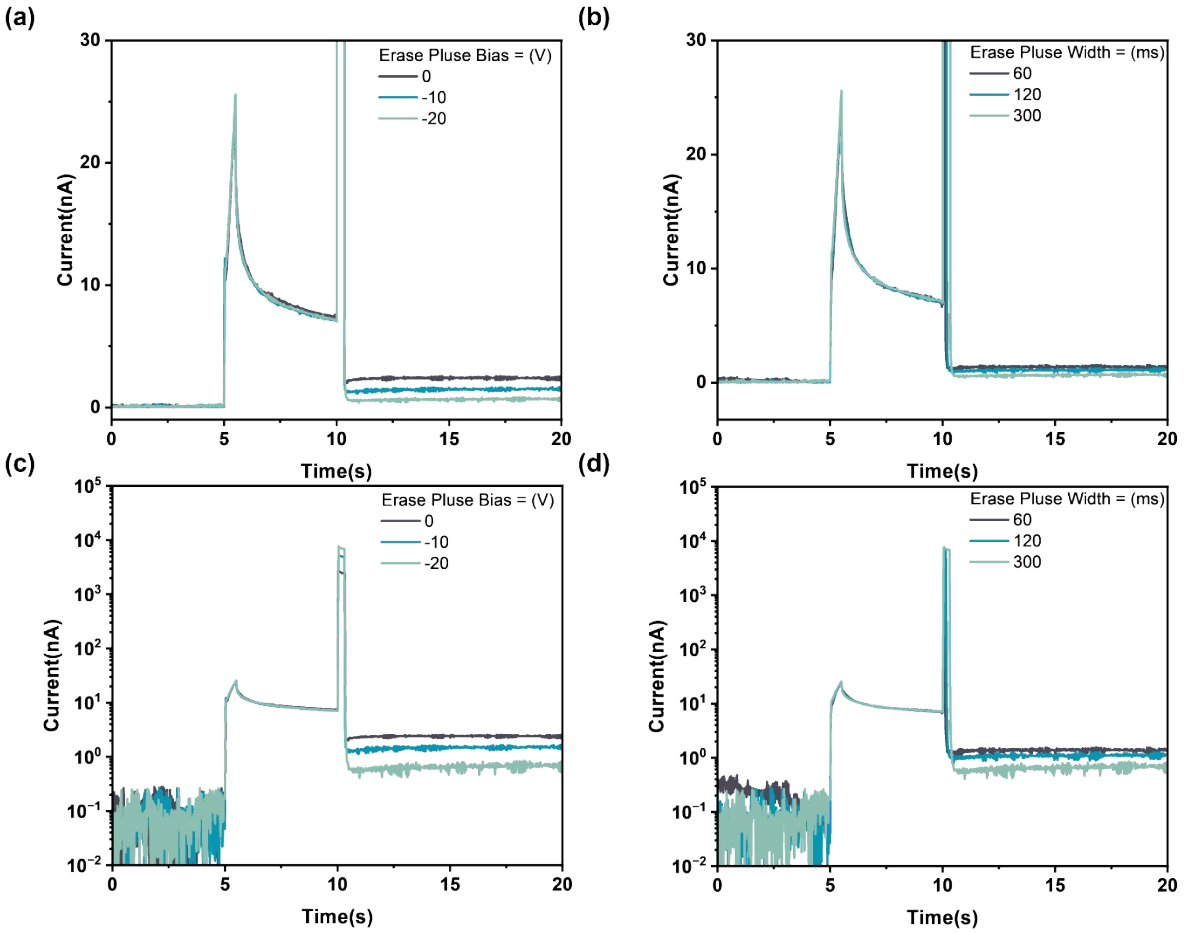


**Fig. S7.** Optimization of electrical reset parameters. Effects of (a, c) erase pulse bias ($V_{gs}$) and (b, d) erase pulse width on the photocurrent decay following a "1000" binary optical pulse sequence.

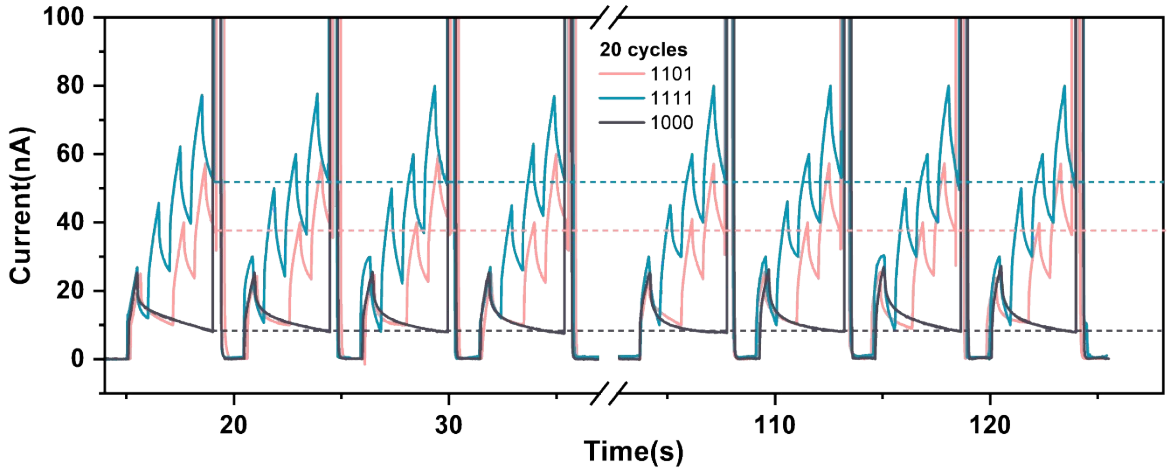


**Fig. S8.** Cyclic operation stability. Photocurrent response over 20 consecutive cycles, where each cycle consists of a 4-bit binary optical pulse sequence (e.g., "1111") followed by an electrical reset pulse ($V_{gs}$ = −20 V, 1 s).

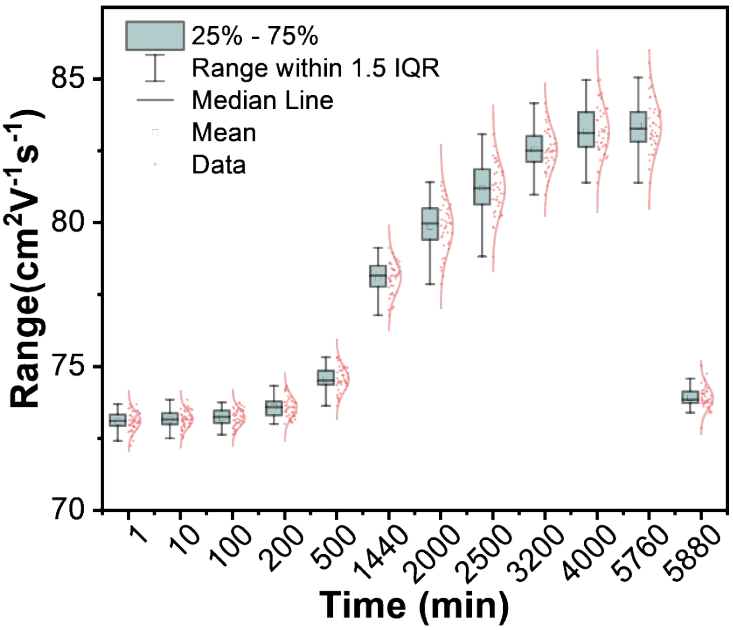


**Fig. S9.** Long-term operational stability. Time-dependent evolution of the photocurrent response to the "1111" optical pulse sequence over extended operation (>5760 min) under ambient conditions (25 °C, 50% relative humidity, dark storage). The arrow indicates thermal re-annealing at 100 °C for 10 min.

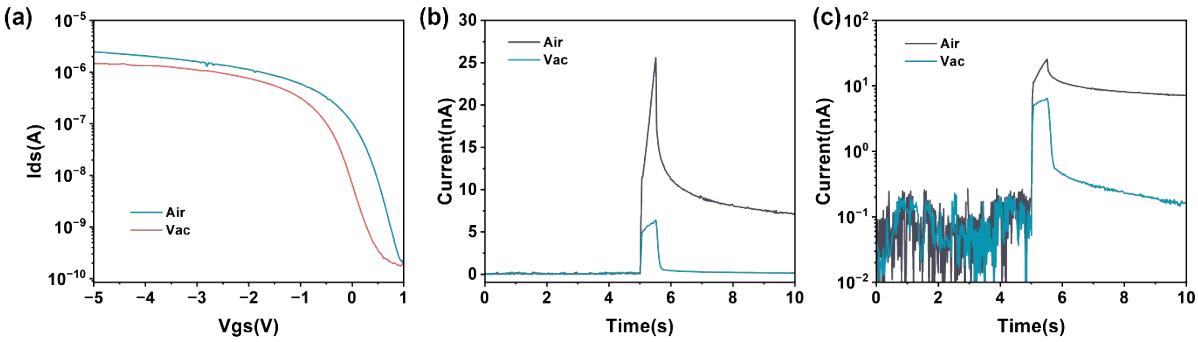


**Fig. S10.** Environment-dependent photoresponse characterization. (a) Transfer characteristics of PDVT-10 OPTs measured in ambient air and high vacuum ($3.3 \times 10^{-4}$ Pa). Pulsed photoresponse curves in (b) linear and (c) semi-logarithmic scales.

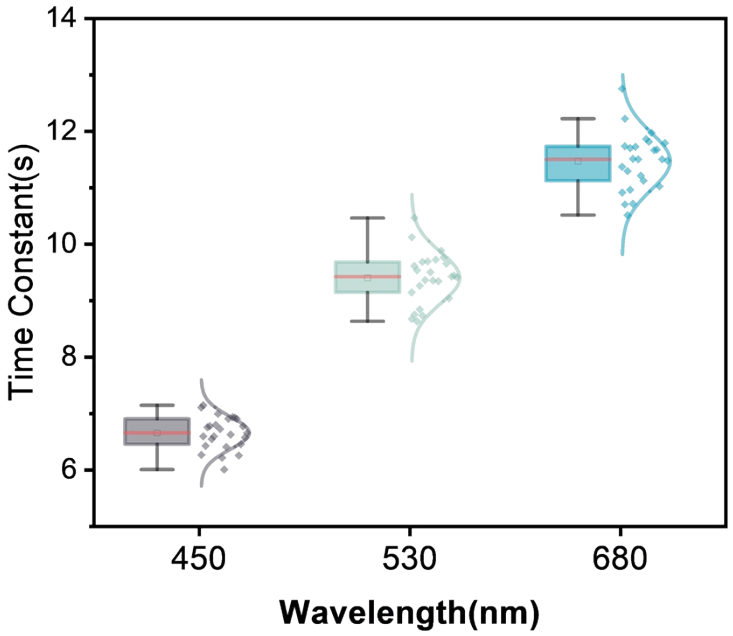


**Fig. S11.** Device-to-device uniformity of decay time constants. Statistical distributions of $\tau_2$ at 450 nm, 530 nm, and 680 nm extracted from bi-exponential fitting of PPC decay curves across 25 devices ($V_{gs}$ = 25 V). The box plots overlaid with individual data points and normal distribution curves illustrate the consistency of the decay dynamics.

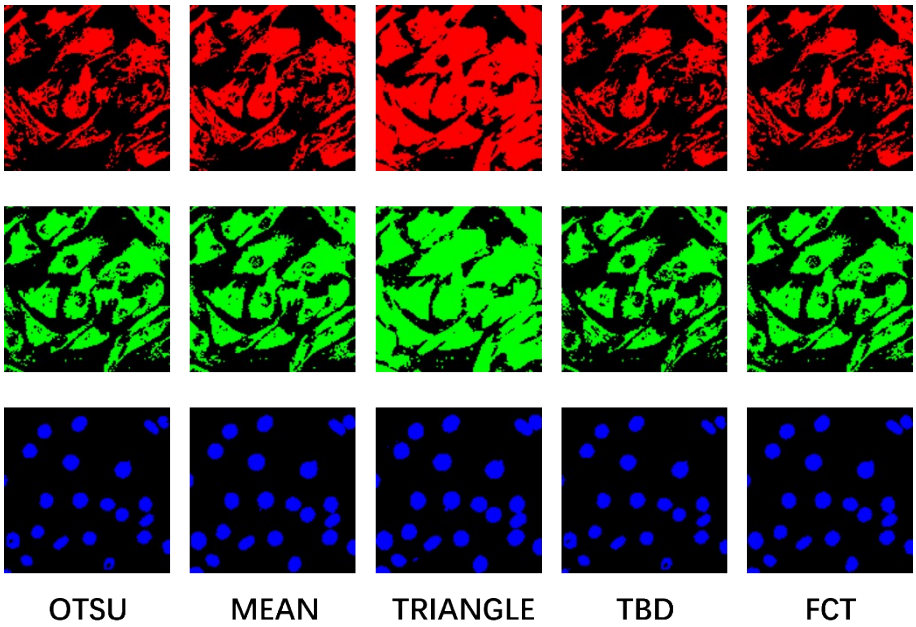


**Fig. S12.** Comparison of binarization methods. Medical fluorescence images from the Human Protein Atlas (HPA) dataset binarized using different methods: time-dependent binarization (TDB), fixed current thresholding (FCT), and software-based methods (Mean, Triangle, Otsu).

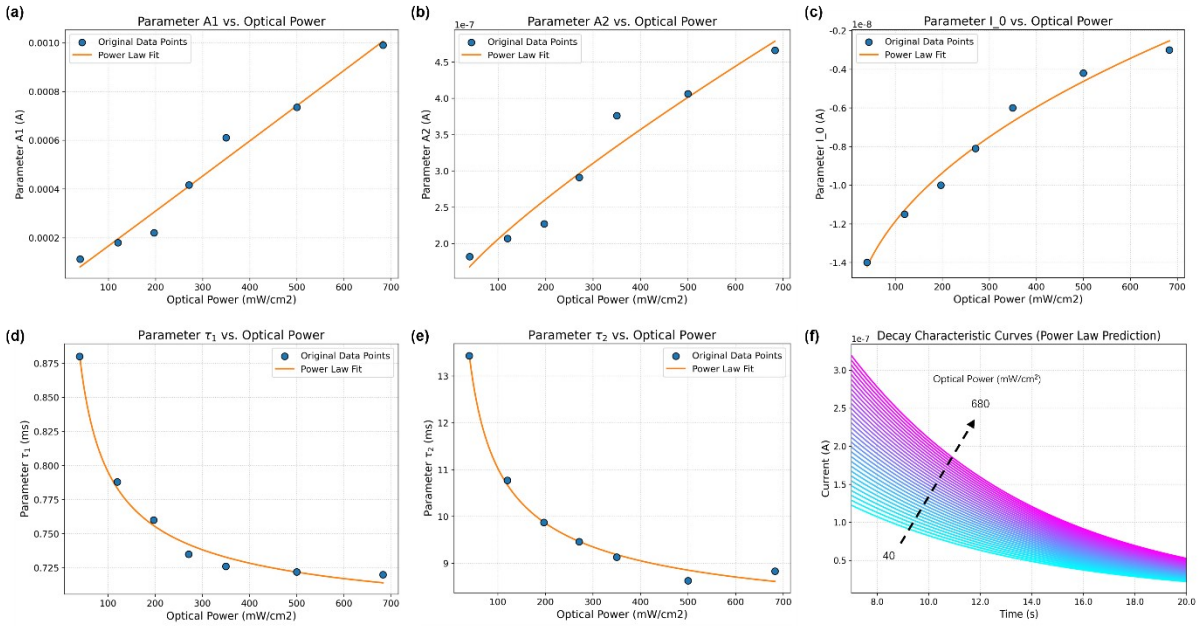


**Fig. S13** Parameter interpolation for decay curve reconstruction. (a-e) Fitting of the five extracted decay parameters ($A_1$,$A_2$,$\tau_1$,$\tau_2$,$I_0$) as a function of optical power (P). Discrete markers represent parameters extracted from experimentally measured decay curves at specific power levels $P_i$, while solid curves show the power-law fits ($\Theta(P) = a \cdot P^b + c$) used for interpolation. (f) Reconstructed photocurrent decay curves at various optical powers (including untested power levels) using the interpolated parameters.

**Table S1. Summary of decay time constants ($\tau_2$) across 25 devices at three wavelengths.**

| Device # | $\tau_2$ (450 nm) | $\tau_2$ (530 nm) | $\tau_2$ (680 nm) | $\tau_R/\tau_B$ |
|---|---|---|---|---|
| 1 | 6.26 | 8.67 | 10.91 | 1.74 |
| 2 | 6.59 | 9.14 | 11.37 | 1.73 |
| 3 | 6.42 | 8.75 | 10.70 | 1.67 |
| 4 | 6.75 | 9.61 | 11.73 | 1.74 |
| 5 | 6.77 | 9.53 | 11.29 | 1.67 |
| 6 | 6.54 | 9.26 | 11.70 | 1.79 |
| 7 | 6.59 | 9.68 | 11.51 | 1.75 |
| 8 | 6.79 | 9.36 | 11.72 | 1.73 |
| 9 | 6.99 | 9.69 | 11.50 | 1.65 |
| 10 | 6.72 | 9.50 | 11.21 | 1.67 |
| 11 | 7.10 | 10.12 | 12.75 | 1.80 |
| 12 | 6.21 | 8.63 | 11.12 | 1.79 |
| 13 | 7.14 | 10.46 | 12.22 | 1.71 |
| 14 | 6.00 | 8.84 | 10.51 | 1.75 |
| 15 | 6.40 | 9.35 | 10.96 | 1.71 |
| 16 | 6.90 | 9.72 | 11.86 | 1.72 |
| 17 | 6.62 | 9.34 | 11.81 | 1.78 |
| 18 | 6.93 | 9.88 | 11.97 | 1.73 |
| 19 | 6.92 | 9.76 | 11.66 | 1.68 |
| 20 | 6.90 | 9.65 | 11.67 | 1.69 |
| 21 | 6.25 | 9.04 | 11.02 | 1.76 |
| 22 | 6.45 | 8.73 | 10.71 | 1.66 |
| 23 | 6.77 | 9.42 | 11.50 | 1.70 |
| 24 | 6.57 | 9.44 | 11.79 | 1.79 |
| 25 | 6.65 | 9.41 | 11.48 | 1.73 |
| **Mean** | **6.60** | **9.35** | **11.60** | **1.76** |
| **S.D.** | **0.29** | **0.46** | **0.51** | **0.05** |
| **CV** | **4.35%** | **4.86%** | **4.46%** | **2.66%** |

**Note S1 XPS and FT-IR Analysis of PDVT-10 Film**

For XPS measurements, devices were exposed to air for 30 min before being transferred to the vacuum chamber for in-situ photoirradiation testing, the result was shown in **Fig. 2c** and **Fig. S5**. In the dark, the C1s spectrum of the PDVT-10 film was dominated by C=C, C-S, and C-N bonds, as expected from its pristine, theoretically oxygen-free structure. However, the O1s spectrum indicated the presence of physisorbed oxygen and/or water molecules on the surface, which may be attributed to not being long enough to completely remove water and oxygen molecules from the film during the vacuum process. Upon illumination, a prominent C-O peak emerged at a high binding energy (286.9 eV) in the C1s spectrum. Concurrently, the signal intensity of component corresponding to chemically bonded oxygen (~532.5 eV, C-O/C=O) increased. These changes indicate that photo-generated electrons are trapped by surface-adsorbed oxygen, triggering a chemical oxidation of the polymer[1].

For FT-IR measurements, the film was irradiated with UV light in air for 1 min, followed by immediate analysis, the result was shown in **Fig. S6**. The FT-IR spectrum after photoirradiation showed significant changes, most notably the appearance of new absorption peaks in the C=O region (1650–1730 $cm^{-1}$). These features correspond to the formation of carbonyl groups (e.g., ketones, aldehydes, or acids/esters). In contrast, the C=C and C–O regions (1000–1300 $cm^{-1}$) remained largely unchanged, suggesting the polymer's main conjugated backbone was preserved[2].

The XPS and FT-IR results are in excellent agreement, confirming that PDVT-10 thin film creates a significant number of carbonyl defects. Since the main chain conjugation is intact, these carbonyl defects are identified as the primary source of deep-level electron traps, which cause the device's PPC behavior[3].

**Note S2. Reconstruction and Physical Basis of Power-Dependent Decay Characteristics**

**S2.1. Methodology for Decay Curve Reconstruction**

To reconstruct decay curves at untested optical power levels ($P$), we employed a two-step parameter interpolation method.

First, experimentally measured decay curves at discrete power levels ($P_i$) were parameterized by fitting them to a double-exponential function, yielding five parameters ($A_1$,$A_2$,$\tau_1$,$\tau_2$,$I_0$) for each $P_i$.

$$I(t) = A_1 e^{-t/\tau_1} + A_2 e^{-t/\tau_2} + I_0$$

Second, the power-dependent relationship of each parameter (e.g., $A_1(P)$) was established by fitting the discrete $(P_i, Param_i)$ data points to a power-law function ($Param(P) = aP^b + c$), generating five continuous functions (shown in **Fig. S13 a-e**).

Finally, these functions were used to interpolate the parameter set $\{\theta_{new}\}$ for any untested power $P_{new}$. These parameters were substituted back into double-exponential function to reconstruct the full decay curve (**Fig. S13 f**), which was subsequently used for effective threshold calculations.

**S2.2. Physical Interpretation of Parameter Trends**

The observed parameter trends are consistent with photophysics dominated by carrier trapping and recombination dynamics in synaptic devices[4].

(1) $A_1$,$A_2$ (Amplitudes): These terms increase (sub-)linearly with $P$, corresponding to the proportional increase in photogenerated carriers captured by shallow ($A_1$) and deep ($A_2$) traps.

(2) $\tau_1$,$\tau_2$ (Time Constants): These lifetimes (fast/shallow traps and slow/deep traps, respectively) decrease as $P$ increases. This is attributed to accelerated carrier recombination dynamics (e.g., $R \propto n^2$) and trap-filling effects at the higher carrier concentrations ($n$) generated by stronger optical power.

(3) $I_0$ (Baseline/PPC): This persistent current ($t \to \infty$) rises with $P$ but exhibits clear saturation. This indicates the progressive filling of a finite density of ultra-deep traps responsible for the Persistent Photoconductivity (PPC) effect. This saturation behavior mimics the hard bounds (upper/lower limits) of biological synaptic weights.

**Note S3. Detailed Mathematical Framework for Time-Dependent Binarization**

**S3.1. Bi-exponential Decay Model**

The temporal dynamics of the photocurrent decay in PDVT-10 OPT are accurately described by a bi-exponential model (as presented in the main text, Fig. 3a):

$$I(t) = A_1 e^{-t/\tau_1} + A_2 e^{-t/\tau_2} + I_0$$

where $\tau_1$ and $\tau_2$ represent the fast and slow time constants, respectively; $A_1$ and $A_2$ represent the amplitude coefficients; and $I_0$ is the steady-state baseline current. The fast component ($\tau_1$, typically ~0.3-1 s) is attributed to the photoconductive (PC) effect and detrapping from shallow trap states, while the slow component ($\tau_2$, typically ~6-12 s) originates from the photogate (PG) effect associated with deep oxygen-induced trap states.

**S3.2. Derivation of Effective Threshold from Inverse Decay Function**

The time-dependent binarization (TDB) strategy implicitly defines an effective threshold $I_{\text{eff},\lambda}$ for each wavelength channel $\lambda$. This effective threshold represents the minimum initial photocurrent required such that, after decaying for the optimized decay time $T_d$, the current remains above a global threshold $I_{\text{th,global}}$. For a given wavelength $\lambda$ and optical power $P$, the photocurrent at time $T_d$ is:

$$I(T_d, \lambda, P) = A_1(\lambda, P) \cdot e^{-T_d/\tau_1(\lambda)} + A_2(\lambda, P) \cdot e^{-T_d/\tau_2(\lambda)} + I_0(\lambda, P)$$

The effective threshold is defined as the optical power $P^*$ (or equivalently, the corresponding initial current $I_{\text{eff}}$) at which $I(T_d,\lambda,P^*) = I_{\text{th,global}}$. Because the decay parameters $\{\tau_1,\tau_2,A_1/A_2\}$ are wavelength-

dependent, the effective thresholds naturally form an ordering: $I_{\text{eff,B}} > I_{\text{eff,G}} > I_{\text{eff,R}}$, which precisely compensates for the device's non-uniform spectral response.

**S3.3. Mathematical Proof of Non-Proportional Threshold Scaling**

A critical property that enables TDB optimization is that the effective threshold ratios are non-proportional functions of $T_d$. Consider the ratio of effective thresholds between two wavelength channels $\lambda_1$ and $\lambda_2$:

$$\frac{I_{\text{eff},\lambda_1}(T_d, P_1)}{I_{\text{eff},\lambda_2}(T_d, P_2)} = \frac{A_1(\lambda_1, P_1) \cdot e^{-T_d/\tau_1(\lambda_1)} + A_2(\lambda_1, P_1) \cdot e^{-T_d/\tau_2(\lambda_1)} + I_0(\lambda_1, P_1)}{A_1(\lambda_2, P_2) \cdot e^{-T_d/\tau_1(\lambda_2)} + A_2(\lambda_2, P_2) \cdot e^{-T_d/\tau_2(\lambda_2)} + I_0(\lambda_2, P_2)}$$

where $P_1$ and $P_2$ denote distinct optical power levels. This ratio is a complex function of $T_d$ because: (1) the exponential decay rates differ between channels ($\tau_1(\lambda_1) \neq \tau_1(\lambda_2)$), (2) the amplitude ratios $A_1/A_2$ vary with wavelength, and (3) the non-zero baseline contributions $I_0$ introduce additional $T_d$-independent terms. Because this ratio is $T_d$-dependent (not constant), different values of $T_d$ produce different relative threshold orderings and spacing. The optimization of $T_d$ therefore identifies the temporal point at which the dynamically adjusted set of adaptive thresholds achieves optimal collective binarization fidelity across all three channels. As shown in Fig. 4d of the main text, the effective threshold curves for different wavelengths converge at short $T_d$ and diverge at longer $T_d$, demonstrating this non-trivial $T_d$-dependence.

**References**


1 Y. Huang, K. Wu, Y. Sun, Y. Hu, Z. Wang, L. Yuan, S. Wang, D. Ji, X. Zhang, H. Dong, Z. Gong, Z. Li, X. Weng, R. Huang, Y. Cui, X. Chen, L. Li and W. Hu, *Nat. Commun.*, 2024, **15**, 626.

2 S. Bellani, D. Fazzi, P. Bruno, E. Giussani, E. V. Canesi, G. Lanzani and M. R. Antognazza, *J. Phys. Chem. C*, 2014, **118**, 6291–6299.

3 R. Jia, X. Wu, W. Deng, X. Zhang, L. Huang, K. Niu, L. Chi and J. Jie, *Adv. Funct. Mater.*, 2019, **29**, 1905657.

4 K. Czerniak-Łosiewicz, A. P. Gertych, M. Świniarski, J. Judek and M. Zdrojek, *J. Phys. Chem. C*, 2020, **124**, 18741–18746.